6.8

Shallow Cellular Convection in Orographic Precipitation

Daniel J. Kirshbaum*and Dale R. Durran
University of Washington, Seattle, WA

1 INTRODUCTION

A range of mechanisms exist for the formation of rainfall upwind of a mountain barrier. Two of the more commonly considered mechanisms are (1) stable, smooth upslope flow and (2) deep convective triggering, in which orographic ascent causes latently unstable air to reach its level of free convection (Banta 1990). Another important means by which orographic precipitation may be generated is through shallow, cellular orographic convection, which involves the development of turbulent convective cells within a preexisting cap cloud formed by upslope orographic flow. The presence of static instability—and the potential for convection to develop—inside such a cloud can be determined by evaluating the sign of the moist Brunt-Väisäla frequency (N_m^2) in the saturated region (Emanuel 1994). While a negative value of N_m^2 indicates statically unstable conditions, this parameter alone does not completely determine whether obvious cellular features will develop in the orographic cloud. Several other factors, such as the residence time of air parcels in the cloud, the depth of the unstable layer, and the basic-state wind profile, may profoundly modulate—or completely suppress—the formation of convective cells.

In this study an investigation of shallow orographic convection will be performed using data from both numerical simulations and real-world observations. Fundamental differences between 2D and 3D simulations in the representation of this convection are shown, along with the effects of different basic-state wind shear profiles on the orientations of the convective cells. In addition, the effects of numerical resolution and frictional dissipation on the 3D convective structures are examined. Finally, a case study involving post-frontal flow over the coastal mountains in western Oregon is presented, illustrating the relation between numerical simulation results and observations.

* *Corresponding author address:* Daniel Kirshbaum; Department of Atmospheric Sciences; University of Washington, Box 351640; Seattle, WA 98195; email:dank@atmos.washington.edu

2 NUMERICAL MODEL

The numerical model used for this analysis is based on Durran and Klemp (1983) and Epifanio and Durran (2001). This cloud-resolving model is nonlinear, non-hydrostatic, fully compressible, inviscid, and uses a terrain-following coordinate system. The subgrid-scale turbulence formulation is based on Lilly (1962), warm-rain microphysics are included through a Kessler parameterization, and a frictional boundary layer is parameterized using first-order closure (Zhang and Anthes 1982). Ice microphysics are neglected for simplicity—and because cloud tops in most of the simulations considered in this paper barely extend to the freezing level. Simulations will be performed in both 2D and 3D.

The upstream thermodynamic profile used for the majority of the simulations is a smoothed version on the 16:47 UTC Milan sounding from 25 September 1999, taken during IOP3 of the MAP field project, during which a substantial amount of cellular convection was observed (Bougeault et al 2001). The skew-T plot for this sounding is shown in Fig. 1a, which indicates a well-mixed layer from the surface to around 900mb, with a layer of decreasing humidity up to 550mb, topped by a shallow inversion. At low levels this sounding is potentially unstable ($d\theta_e/dz < 0$), which can be seen from the θ_e profile in Fig. 1b. The idealized basic-state wind profile (Fig. 1c) exhibits parallel shear, with the zonal wind rising linearly from 10 ms^{-1} at the surface to 40 ms^{-1} at 9km, then remaining constant at 40 ms^{-1} to the top of the domain.

3 2D VS. 3D COMPARISON

The inclusion of the third spatial dimension is necessary for realistic simulations of airflow over topography because this allows air to flow around, as well as over, an isolated mountain. In addition, it allows convective circulations to develop around ar-

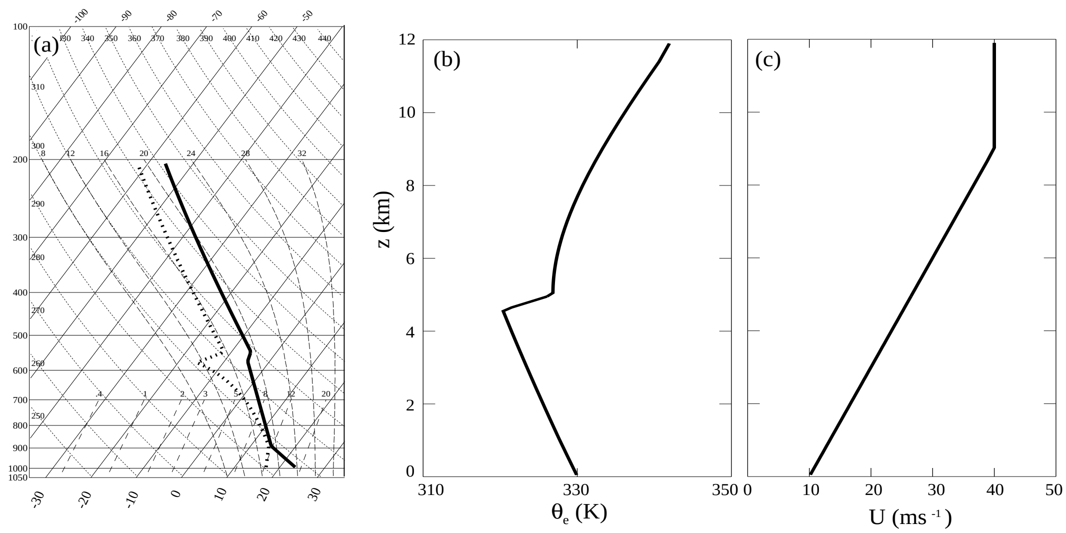

Figure 1: Smoothed IOP3 sounding used for control experiments. (a) Skew-T plot, (b) θ_e profile, and (c) $U(z)$ profile.

bitrary axes of rotation. To isolate the effects of three-dimensionality on the cellular structure of orographic clouds, two simulations are compared which are essentially identical except that while the former (IOP3-2D) is performed in 2D, the latter (IOP3-inf) has a uniform ridge and periodic boundaries in the cross-flow direction, thereby representing an infinite barrier. Both simulations, which employ the smoothed IOP3 sounding described above, have horizontal grid spacings of 600m and vertical grid spacings of 100m from the surface to 5km, stretching linearly to 400m at 10km, then remaining constant to the top of the domain. The mountain profile for both simulations has a peak height (H) of 1.5km at the center of the domain and horizontal half-width (a_x) of 20km in both the upstream and downstream directions. In addition, uniformly distributed bumps of amplitude $A_n = 15$m (with $2\Delta x$ component filtered out) have been added to the upslopes of the mountains to create perturbations of finite amplitude which may ultimately develop into cellular features. Fig. 2 shows that, in certain vertical cross sections, no major differences are apparent between the 2D (Fig. 2a) and 3D (Fig. 2b) simulations. Nevertheless, Fig. 3 indicates that the 3D simulation has actually developed an organized pattern of longitudinal bands (Fig. 3a) with a clear circulation parallel to the mean wind axis (Fig. 3b). These convective features greatly increase the intensity, accumulation, and efficiency of precipitation produced by the 3D orographic cloud over that of the 2D cloud, in which convection is strongly suppressed by the basic-state shear. The maximum rainfall rate and precipitation efficiency over the interval $0 < t \leq 16,200$s increase from 6.9 to 77.8 mmhr^{-1}, and 39.6% to 72.9%, respectively, and the total area-averaged surface rainfall at $t = 16,200$s rises from 0.73 to to 1.56mm when the third dimension is added to the analysis.

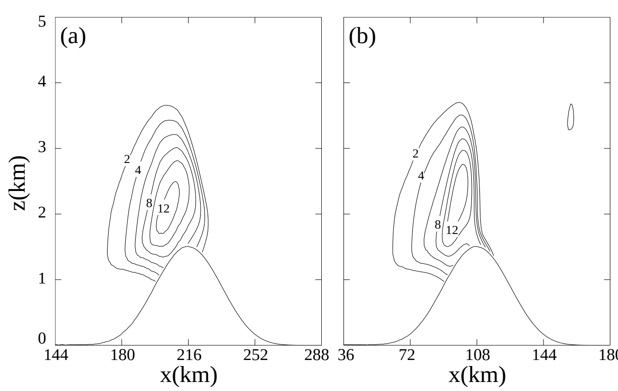

Figure 2: Cloud water fields at 8100s for (a) IOP3-2D simulation and (b) IOP3-inf simulation at $y = 12$km. Contour labels are multiplied by 10^{-4}.

4 EFFECTS OF INCREASING NUMERICAL RESOLUTION

Numerical resolution is a critical parameter for the accurate representation of explicit atmospheric convection, which, due to its turbulent nature, contains energy at scales which are too small to model explicitly. To determine the effects of numerical resolution on the structure of convective elements such as those

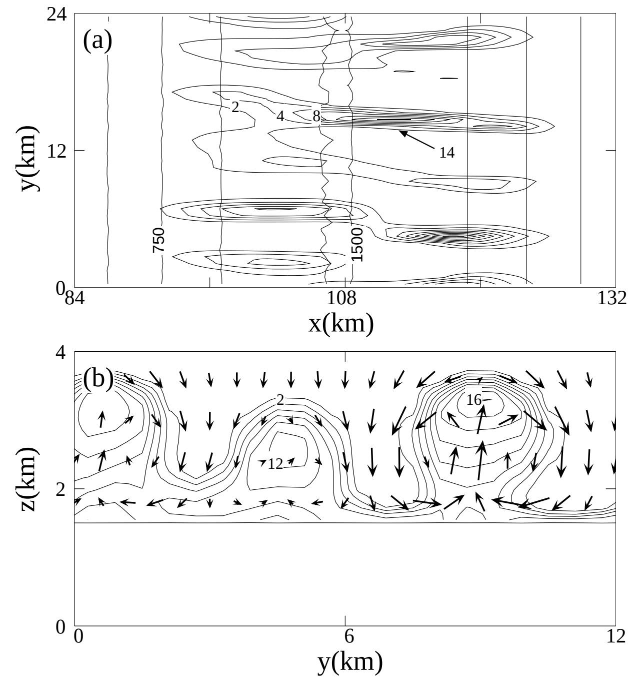

Figure 3: IOP3-q2D simulation at $t = 8100$s. (a) Surface q_r field and (b) q_c field at $x = 108$, overlaid with scaled velocity contours, along the mountain crest. Contour labels for q_c are multiplied by 10^{-4}, labels for terrain are in meters

seen in Fig. 3, three simulations are compared which are identical except for their different horizontal grid spacings. For these simulations, which employ the same sounding profile and basic terrain properties (H, a_x, and A_n) as those of the previous section, three-level, two-way grid nesting has been employed to reduce computational expense. The finest grid has been placed around the finite-length ridge, which along the centerpoint ($x = 216$km) has a length of 60km and half-width (a_y) of 10km, in such a way as to allow the convective motions in the cloud to be analyzed at the highest resolution. The first simulation (IOP3-600) has a horizontal grid spacing of 600m on the finest grid, and 1.8km and 5.4km on the two coarser grids; the second simulation (IOP3-400) has horizontal grid spacings of 400m, 1.2km, and 3.6km on the three grids; the final simulation (IOP3-200) uses four grids and has spatial resolutions of 200m, 600m, 1.8km, and 5.4km. A comparison of the surface rainwater mixing ratios (q_r) of these simulations after 2.25h ($t = 8,100$s) of run time is provided in Fig. 4. As the resolution is progressively increased, the distance between adjacent updrafts—and width of the updrafts themselves—decreases. This result illustrates the dependence that convective features may have upon horizontal resolution in inviscid numerical simulations.

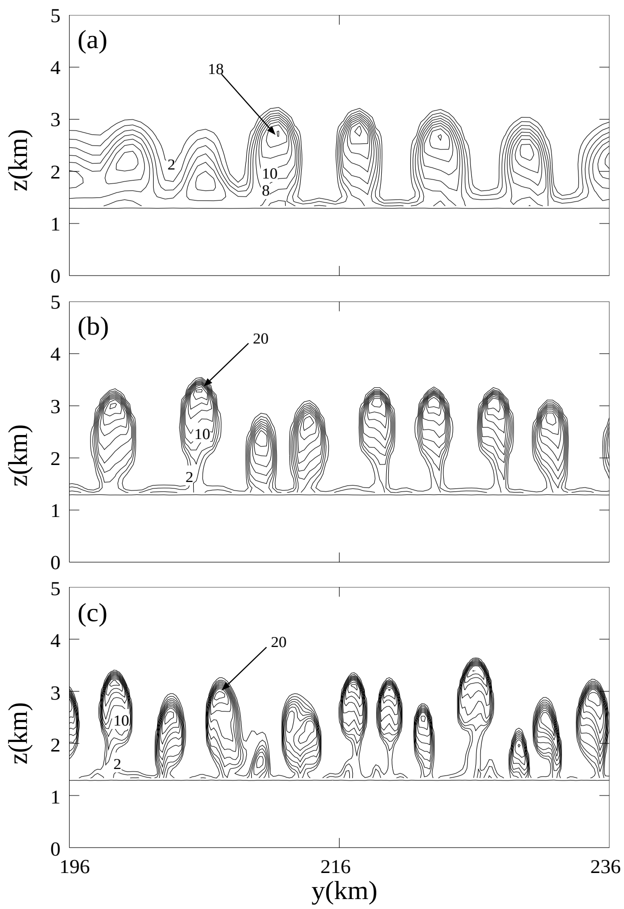

Figure 4: Surface q_r comparison of simulations with different numerical resolutions at $t = 8,100$s. (a) $\Delta x = \Delta y = 600$m, (b) $\Delta x = \Delta y = 400$m, (c) $\Delta x = \Delta y = 200$m. Contour labels are multiplied by 10^{-4}.

5 FRICTIONAL DISSIPATION

Because viscous effects tend to dissipate energy on the small scales at which turbulent eddies develop, the addition of a boundary layer parameterization enforcing a no-slip surface condition may be expected to modulate the features of the convective bands seen in free-slip simulations. A comparison of three simulations at $t = 16,200$s identical to those of Section 4 except for the presence of a frictional boundary layer over the mountain ridge is provided in Fig. 5. As in the previous comparison, the updraft width and spacing are reduced as the horizontal resolution is increased from 600m (Fig. 5a) to 400m (Fig. 5b). However, as the resolution is increased further to 200m (Fig. 5c), no additional decrease is apparent in these features, in spite of the fact that smaller-scale details within the clouds are clearly better resolved in the 200m simulation. Here the viscous dissipation introduced by the frictional boundary layer has acted to decouple the gross characteristics of the convective rainbands from the horizontal grid spacing. Because of the qualitative similarities between the cloud formations in Figs. 5b and 5c, we can conclude that a horizontal resolution of 400m is sufficient to resolve the primary convective features in this example.

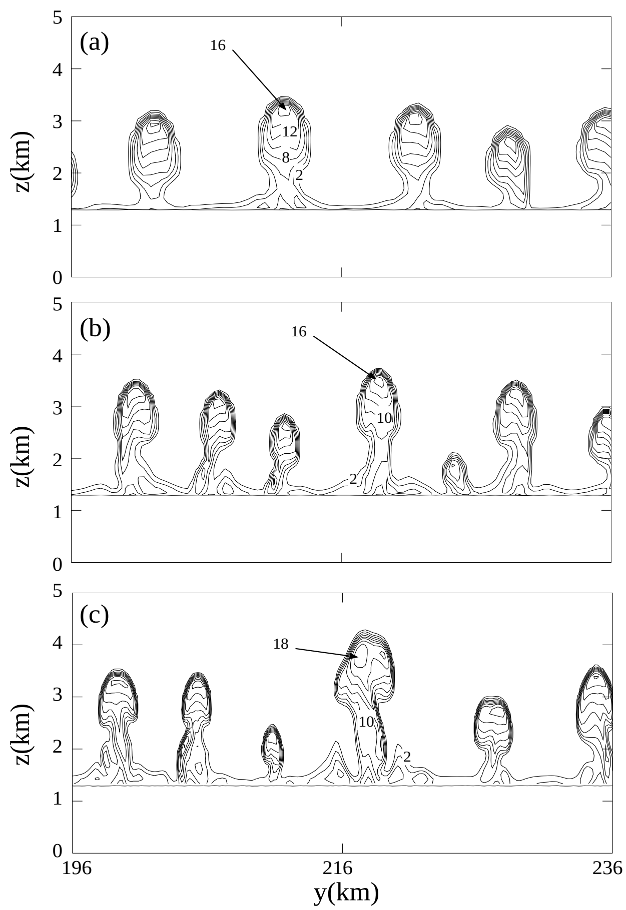

Figure 5: Surface q_r comparison of simulations with frictional boundary layers and different numerical resolutions at $t = 16,200$s. (a) $\Delta x = \Delta y = 600$m, (b) $\Delta x = \Delta y = 400$m, (c) $\Delta x = \Delta y = 200$m. Contour labels are multiplied by 10^{-4}.

6 PARALLEL VS. DIRECTIONAL SHEAR

To examine the influence of the basic-state wind in determining the orientation of convective bands such as those seen in Figs. 3-5, two simulations are compared with different basic-state wind profiles. The first simulation (IOP3-400) is the parallel shear flow with 400m grid spacing from Section 3, while the second (IOP3-turn) is identical to IOP3-400 except that now both $U(z)$ and $V(z)$ have linear shear profiles up to 9km. $V(z)$ has a value of -10ms^{-1} at the surface, rising to 20ms^{-1} at 9km, then remaining constant to the top of the domain. The resulting basic-state wind profile has a surface direction of 135° (measured counter-clockwise from the positive $y-$axis) and a shear vector direction of 45°. The surface q_r fields at $t = 5670$s are compared in Figs. 6a and 6b, indicating convective rainbands oriented roughly parallel to the basic-state shear vectors in both simulations, with the bands in IOP3-turn containing significantly less rainwater than those in IOP3-400. At a later time ($t = 8100$s), Fig. 6c shows that IOP3-400 maintains its vigorous streamwise convective bands, while in IOP3-turn (Fig. 6d) the shear-parallel features have vanished, replaced by even weaker bands aligned with the mean wind vector in the cloud layer. This comparison suggests that while convective features may align themselves with either the basic-state wind or shear vector in the cloud layer, the most intense and long-lived modes occur when the mean wind and shear are parallel.

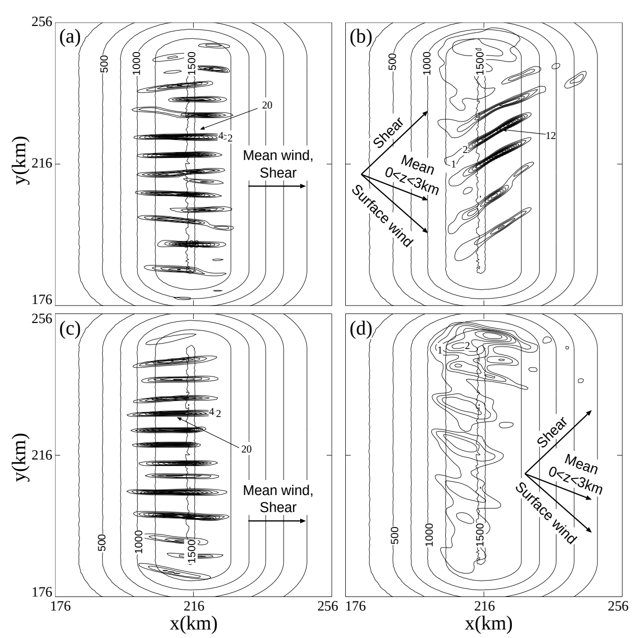

Figure 6: Shear comparison. Surface q_r fields at $t = 5670$s for (a) IOP3-400 simulation and (b) IOP3-turn. Surface q_r fields at $t = 8100$s for (c) IOP3-400 and (d) IOP3-turn. Contour labels for q_c are multiplied by 10^{-4}, labels for terrain are in meters

7 REAL DATA CASE

The numerically-generated results from the previous sections suggest that, under certain conditions, parallel convective bands may develop in upslope orographic flow with a well-defined orientation, width, and horizontal spacing. In this section a real-world example of convective rainbands similar in character to those examples will be presented, along with a comparison between the observed features and those of an idealized simulation of the orographic rain event. The case study involves post-cold-frontal upslope flow over the coastal mountains of western Oregon between 20:00 UTC on 12 Nov. 2002 and 02:00 UTC on 13 Nov. 2002. A radar image of base reflectivity from the Portland, OR NEXRAD station at 21:50 UTC is shown in Fig. 8a, indicating rainbands oriented linearly over the coastal range; these rainbands persisted over this region with the same general character for over six hours. The upstream conditions during this rain event, represented by a composite of thermodynamic data from Quillayute, WA and wind data from both Salem, OR and Newport, OR at 00Z on 13 Nov. 2002, are shown in Fig. 7. From Fig. 7b it is evident that a layer of potential instability is present below 3km, while the wind profile in Fig. 7c exhibits a southwesterly flow with nearly parallel shear in the 1-3km layer. This sounding has been used in a numerical simulation employing a frictional boundary layer and a finite-length mountain identical to that of Sections 4 and 5 except that $H = 1$km to better represent the Oregon coastal range. The base reflectivity at $t = 16,200$s and $z = 1.2$km, calculated from the bulk liquid water fields using an empirical formula from Douglas (1964), is shown in Fig. 8b. Here streamwise-oriented rainbands are evident which are similar in character to those in the radar image from Fig. 7a. While the characteristic orientations ($\sim 33°$), rainband widths ($\sim$ 3km), and maximum reflectivities ($\sim$ 45dBZ) are nearly identical between the two figures, the mean spacing between the bands is considerably less for the simulated (4km) than for the observed (7km) event. A possible explanation for this discrepancy derives from the idealized topographic profile used in the numerical simulation. Because this profile is free of large-scale irregularities and isolated peaks, the convective rolls take on a natural organization associated with the most energetic modes. However, in actual flow over rugged terrain, the enhanced upward motion in the vicinity of isolated peaks may focus the convective activity in those regions, prevented the natural spacing from being achieved in many areas.

8 SUMMARY

In this study it has been shown that linearly-oriented convective rainbands may develop when moist shear flows with shallow layers of potential instability ascend orographic obstacles. Data from numerical simulations using realistic sounding profiles indicate that three dimensions are necessary to produce the convective circulations that give rise to these rainbands, which greatly enhance the precipitation intensity, accumulation, and efficiency over that of 2D simulations, in which convection is suppressed by the shear. The main features of these rainbands, such as updraft width and spacing, depend strongly on horizontal resolution in inviscid simulations. In the presence of frictional dissipation with sufficient resolution, however, this dependence appears to be greatly reduced, and a resolution of 400m appears sufficient to capture the main features of the convective circulations in this case. The alignment and intensity of the rainbands was shown to depend on the relationship between the mean wind in the cloud layer and the vertical shear of the basic-state wind; parallel shear flows produce intense, long-lived streamwise rainbands, differing greatly from the weaker and more transient shear and mean-wind-parallel rainbands in the directional shear case.

To bridge the gap between idealized numerical simulations and reality, an example of shallow convective rainbands from a case of potentially unstable upslope flow over the coastal mountains in western Oregon was analyzed and compared to a numerical simulation of the rain event. The observed convective bands in this case shared many characteristics in common with the numerical simulation, suggesting that the features seen in model data have real-world significance. More such examples are necessary to reinforce this result and enhance the understanding of the environmental and terrain-related factors which regulate the development and properties of convective orographic rainbands.

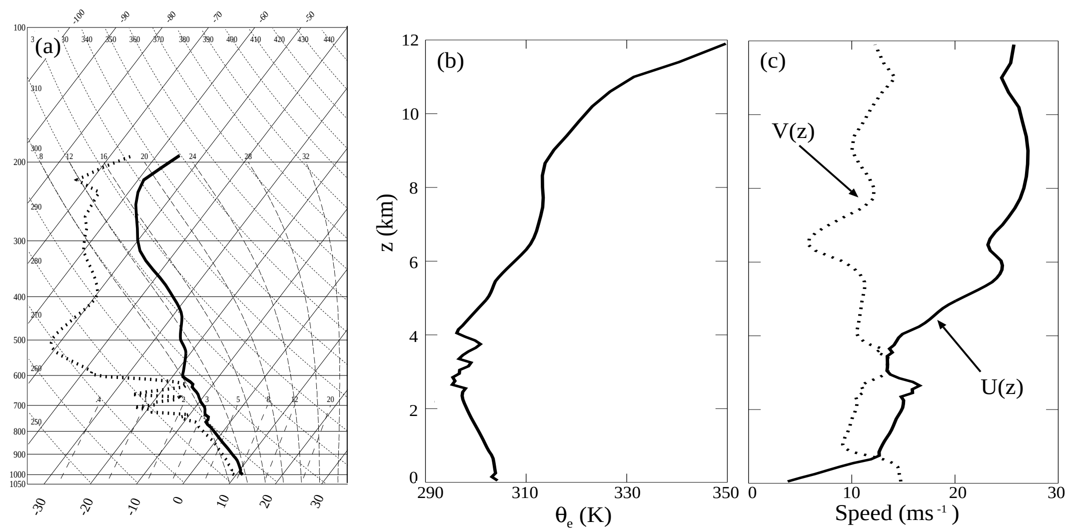

Figure 7: Composite sounding used for real data case. (a) Skew-T plot and (b) θ_e profile from from Quillayute, WA and (c) Mean wind $U(z)$ and $V(z)$ profiles from Salem, OR and Newport, OR on on 00Z, 13 Nov. 2002.

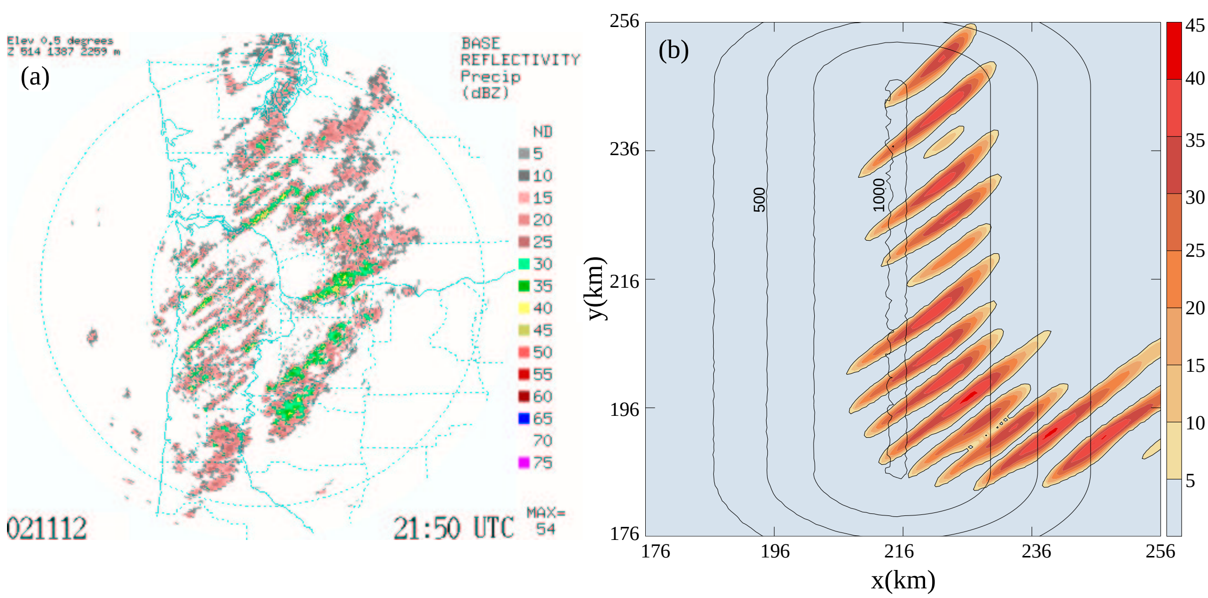

Figure 8: Comparison between observational and numerically-simulated data. (a) Portland, OR NEXRAD reflectivity data from 2150 UTC, 12 Nov. 2002, (b) reflectivity from numerical simulation using sounding data from Fig. 7 at $t = 16,200$s, calculated using empirical formula. Contour labels multiplied by 10^{-4} for q_c, labels for terrain are in meters

References

[1] Banta, R.M., 1990: Atmospheric processes over complex terrain. *Meteorological Monographs*, W. Blumen, Ed., **23**, American Meteorological Society, 229-283.

[2] Bougeault, P., P. Binder, A. Buzzi, R. Dirks, R. Houze, J. Kuettner, R.B. Smith, R. Steinacker, and H. Volkert, 2001: The MAP special observing period. *Bulletin of the American Meteorological Society* **82**, 433-462.

[3] Douglas, R.H., 1964: Hail size distribution. Preprints, *11th Conference on Radar Meteorology*. Boulder, American Meteorological Society, 146-149.

[4] Durran, D.R., J.B. Klemp, 1983: A compressible model for the simulation of moist mountain waves. *Monthly Weather Review* **111**, 2341-2361.

[5] Emanuel, K.A., 1994. *Atmospheric Convection*. Oxford University Press, 580 pp.

[6] Epifanio, C.C., and Durran, D.R., 2001: Three-dimensional effects in high-drag-state flows over long ridges. *Journal of the Atmospheric Sciences* **58**, 1051-1065.

[7] Lilly, D.K., 1962: On the numerical simulation of buoyant convection. *Tellus* **14**, 148-172.

[8] Zhang, D., and Anthes, R.A., 1982: A high-resolution model of the planetary boundary layer—sensitivity tests and comparsions with SESAME-79 data. *Journal of Applied Meteorology* **21**, 1594-1609.